Supernova Remnants II: An Odyssey in Space after Stellar death, Chania, Crete, Greece, June 2 – 8, 2019

Revealing the radio continuum and X-ray properties of the Galactic supernova remnant G5.9+3.1 with Murchison Widefield Array and XMM-Newton

D. Onić[1], M. D. Filipović[2], I. Bojičić[2], N. Hurley-Walker[3], B. Arbutina[1], T. G. Pannuti[4], C. Maitra[5], D. Urošević[1], F. Haberl[5], N. Maxted[2, 6], G. F. Wong[2, 6], G. Rowell[7], M. E. Bell[8], J. R. Callingham[9], K. S. Dwarakanath[10], B.-Q. For[11], P. J. Hancock[3], L. Hindson[12], M. Johnston-Hollitt[3], A. D. Kapińska[11], E. Lenc[13], B. McKinley[14], J. Morgan[3], A. R. Offringa[9], L. E. Porter[4], P. Procopio[15], L. Staveley-Smith[11], R. B. Wayth[3], C. Wu[11], and Q. Zheng[16]

donic@matf.bg.ac.rs

ABSTRACT

We discuss here the radio and X-ray properties of the supernova remnant (SNR) G5.9+3.1. The low frequency radio continuum of this Galactic remnant is obtained with the Murchison Widefield Array (MWA). Combining these new data with the surveys at other radio frequencies, we discuss the integrated radio spectrum of this object. The radio spectrum is very well explained by a simple power-law relation with the synchrotron radio spectral index of 0.42±0.03. We also propose that the identified point radio source, located centrally inside the SNR shell, is most probably a compact remnant of the supernova explosion. Finally, an archival XMM-Newton observation is also analyzed and we note the first detection of X-ray emission from this source.

SNR G5.9+3.1

The poorly studied **Galactic SNR G5.9+3.1** was originally identified based on the radio continuum surveys of the Galactic plane with the Effelsberg 100-m telescope at 11/21 cm (Reich et al. 1988). Morphologically, it is a shell remnant with an average angular radius of around 10'. Based on a revised radio surface brightness to diameter relation, Pavlović et al. (2013, 2014) estimated the diameter of this object and its distance, based on the method of orthogonal fitting, to be around 31.2 pc and 5.4±2.8 kpc, respectively.

Combining particular MWA wideband low-frequency observations (see Fig. 1) with the Effelsberg 100-m Galactic plane survey at 1408 MHz and 2695 MHz as well as with the RATAN 600 Galactic plane survey at 960 MHz and 3900 MHz, we present the radio continuum of the SNR G5.9+3.1 (see Fig. 2).

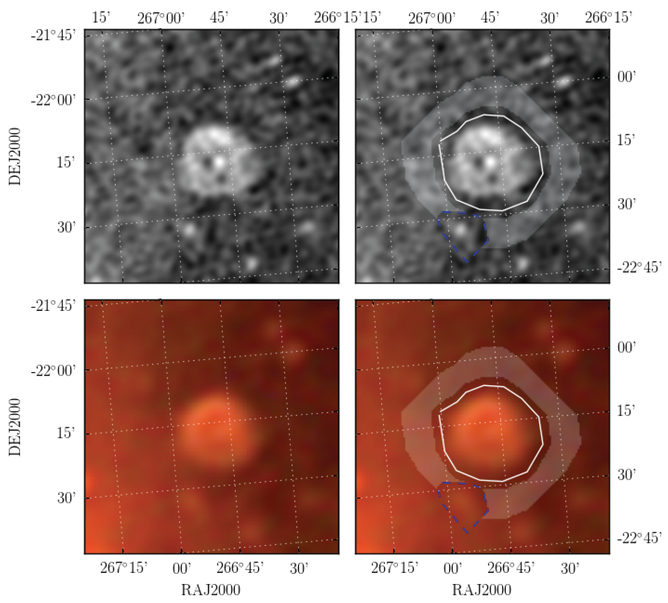

Figure 1. The GaLactic and Extragalactic All-sky Murchison Widefield Array (GLEAM) survey images of G5.9+3.1; the top two panels show the wideband image taken over 170-231 MHz, while the lower two panels show an RGB image comprised of R=72-103 MHz, G=103-134 MHz, B=139-170 MHz. The full width at half maximums of the point spread functions of the images are, respectively: 2.40, 5.20, 3.90, and 2.90. The left panels show the images without any annotations. The right panels show annotations indicating the GLEAM photometry measurement: the white lines show the region drawn by the observer that contains the SNR; the gray shaded region shows the area used to calculate the background; the blue dashed lines show a region excluded from the background measurement for containing contaminating background radio galaxies.

Because of the steep radio spectral index (α=0.99±0.05) and small values of the flux densities for the point radio source, which lay in the center of the SNR shell, we can actually use the MWA, Effelsberg, and RATAN-600 integrated flux densities assuming that the contribution of the central radio source is negligible. As the above 100 MHz the spectra of the majority of detected pulsars can be described just by a simple power law with the average value of spectral index around 1.8 (or from 0.46 to 4.84), **we propose that this central object is possibly the compact remnant of the supernova explosion that gave rise to G5.9+3.1**. This central point radio source is coincident with the position of the long-period variable star known in the OGLE Galactic Bulge LPV star catalogue as OGLE BLG-LPV 38416. However, the non-thermal radio continuum of this point source is not in a good accordance with the optically thick thermal free-free emission from a post-shock partially ionized layer in a stellar atmosphere, or with thermal emission from the stellar photosphere, nor with non-thermal radio emission associated with stellar flare activity.

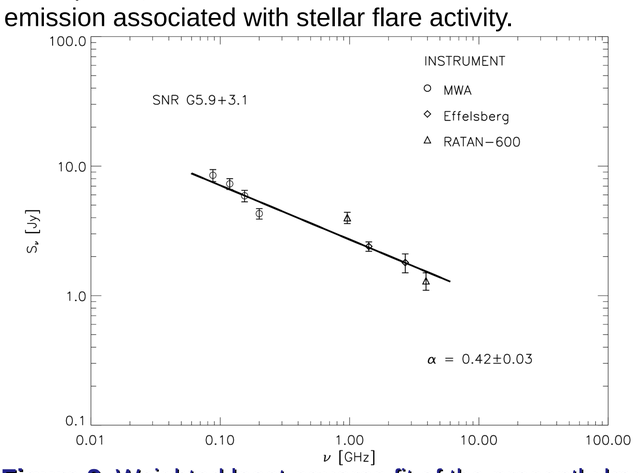

Frequency – ν (MHz)	Telescope	$S_\nu^{\rm SNR}$ (Jy)
072-103 (87.5)	MWA	8.5 ± 0.9
103-134 (118.5)	MWA	7.3 ± 0.7
139-170 (154.5)	MWA	5.9 ± 0.6
170-231 (200.5)	MWA	4.3 ± 0.4
960	RATAN-600	4.0 ± 0.4
1408	Effelsberg	2.4 ± 0.2
2695	Effelsberg	1.8 ± 0.3
3900	RATAN-600	1.3 ± 0.2

Figure 2. Weighted least-squares fit of the presently known integrated radio continuum spectrum of the SNR G5.9+3.1 using the simple power-law model for pure synchrotron emission (left, solid line). Circles correspond to the MWA data, diamond symbols indicate Effelsberg data, and triangles depict RATAN observations. The integrated flux density measurements of SNR G5.9+3.1 (right, table)

X-RAY ANALYSIS

The SNR G5.9+3.1 was the subject of an observation made with the three European Photon Imaging Cameras (EPIC) MOS1, MOS2, and PN aboard the XMM-Newton Observatory on the 1 March 2006 (PI: R. Bandiera; Obs. ID 0553110401). After processing, the effective exposure times of the PN, MOS1, and MOS2 cameras were 6281 seconds, 11040 seconds, and 11080 seconds, respectively. **Using the data collected by all three EPIC cameras, we conducted a spatially resolved spectroscopic analysis of the X-ray emission from G5.9+3.1.** Appropriate source regions (corresponding to the **whole SNR** along with the **east rim**, the **north rim**, and the **west rim**) and background regions were selected taking care to exclude the point sources (see Fig. 3). As the background can have strong spatial variations, the region for extraction of background spectra was selected by averaging over several regions across the detector plane. Two spectra (both for source and background) were extracted per instrument from each region: the first spectrum was extracted from the event list of the science observation and the second spectrum was extracted from the filter wheel closed (FWC) data. The corresponding spectra from the FWC data were subtracted from the science spectra of the source and background regions to **subtract the quiescent particle background** component. The source spectra for each region of interest of G5.9+3.1 and the background spectra from each camera were **fit simultaneously** to constrain the source component (best modeled with the APEC, due to the high ionization age so that CIE is applicable) as well as **the astrophysical background** (AXB) component. We used a three-component model for the AXB: the first component was an unabsorbed thermal component for the local hot bubble (LHB), while the second component was an absorbed thermal component for the Galactic halo emission (Halo). Both of these components were fit with the APEC model with elemental abundances frozen to solar values. The third component was an absorbed power law for the non-thermal unresolved extragalactic X-ray background (DXB).

The full model applied in the spectral fitting can be denoted as:

$$\textbf{CONSTANT} \times (\textbf{APEC}_{\rm LHB} + \textbf{TBABS} \times (\textbf{APEC}_{\rm Halo} + \textbf{Power Law}_{\rm DXB}) + \textbf{TBABS} \times \textbf{APEC}_{\rm Source}).$$

Here, "CONSTANT" refers to multiplicative constants used to account for variations in calibration between the different EPIC cameras and "TBABS" is the Tübingen-Boulder interstellar photoelectric absorption model with solar abundances (see Fig. 4).

Extracted EPIC spectra from the whole SNR as well as the north, east, and west rims of the SNR are fit successfully with **an optically thin thermal plasma model in CIE** with a hydrogen **column density $N_H \sim 0.80 \times 10^{22}$ cm^{-2} and temperatures spanning the range kT ~ 0.14 − 0.23 keV** for all of the regions. The derived electron number densities n_e for the whole SNR and the rims are also roughly comparable **(ranging from ~ 0.20 f$^{-1/2}$ cm^{-3} to ~ 0.40 f$^{-1/2}$ cm^{-3}, where f is the volume filling factor).** We also estimate the swept-up mass of the X-ray emitting plasma associated with G5.9+3.1 to be around 46 f$^{-1/2}$ $M_{\rm sun}$.

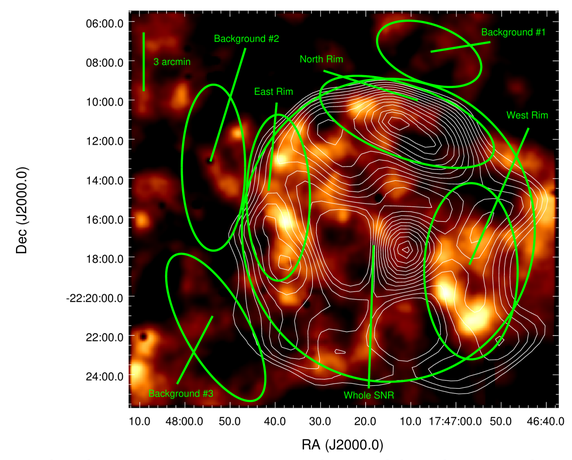

Figure 3. Adaptively smoothed exposure-corrected combined EPIC image of G5.9+3.1. The image depicts emission detected over the energy range 0.4 keV to 1.0 keV. Emission from discrete sources has been flagged and excised in the creation of this image. The contours overlaid depict radio emission detected by the MWA and regions of spectral extraction indicated and labeled. The X-ray emission along the eastern and western rims of G5.9+3.1 appears to lie interior to the radio rims, while X-ray and radio emission from the northern and southern rims are weak or absent. The source regions of spectral extraction for the northern, western, and eastern rims along with the entire SNR are indicated, as well as the accompanying regions of background spectral extraction.

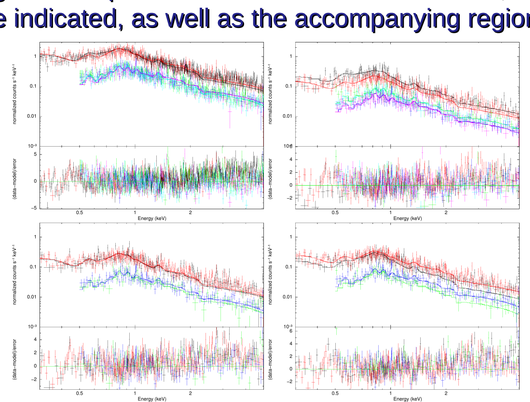

Parameter	Whole SNR	East rim	North rim	West rim
	Source spectrum fit parameters			
$N_{\rm H}$ (10^{22} cm^{-2})	0.80 ± 0.04	$0.75^{+0.07}_{-0.08}$	$0.84^{+0.15}_{-0.09}$	$0.80^{+0.10}_{-0.11}$
kT (keV)	$0.15^{+0.01}_{-0.01}$	$0.14^{+0.03}_{-0.03}$	$0.17^{+0.08}_{-0.06}$	$0.23^{+0.16}_{-0.06}$
Abundance (Solar)	1.00 (Frozen)	1.00 (Frozen)	1.00 (Frozen)	1.00 (Frozen)
Normalization (cm^{-5})	4.15×10^{-2}	5.81×10^{-3}	1.89×10^{-3}	2.40×10^{-3}
	Astrophysical X-ray background spectrum fit parameters			
Constant (PN-SRC)	1.00 (Frozen)	1.00 (Frozen)	1.00 (Frozen)	1.00 (Frozen)
Constant (PN-BKG)	1.00 (Frozen)	1.00 (Frozen)	1.00 (Frozen)	1.00 (Frozen)
Constant (MOS1-SRC)	0.85 (Frozen)	0.85 ± 0.04	0.85 (Frozen)	0.83 ± 0.05
Constant (MOS1-BKG)	0.85 (Frozen)	0.85 ± 0.04	0.85 (Frozen)	0.83 ± 0.05
Constant (MOS2-SRC)	0.85 (Frozen)	0.83 ± 0.04	–	–
Constant (MOS2-BKG)	0.85 (Frozen)	0.83 ± 0.04	–	–
$kT_{\rm Halo}$ (keV)	$0.30^{+0.02}_{-0.01}$	$0.29^{+0.02}_{-0.01}$	$0.28^{+0.02}_{-0.04}$	$0.28^{+0.03}_{-0.04}$
Abundance (Solar)	1.00 (Frozen)	1.00 (Frozen)	1.00 (Frozen)	1.00 (Frozen)
Normalization$_{\rm Halo}$ (cm^{-5})	1.35×10^{-2}	1.58×10^{-3}	2.62×10^{-3}	2.89×10^{-3}
$\Gamma_{\rm DXB}$	1.46 (Frozen)	1.46 (Frozen)	1.46 (Frozen)	1.46 (Frozen)
Normalization$_{\rm DXB}$	1.60×10^{-3}	1.64×10^{-4}	2.1	2.83×10^{-4}
$kT_{\rm LHB}$ (keV)	0.10 (Frozen)	0.10 (frozen)	0.10	.10 (Frozen)
Abundance (Solar)	1.00 (Frozen)	1.00 (Frozen)	1.00 (Frozen)	1.00 (Frozen)
Normalization$_{\rm LHB}$ (cm^{-5})	2.42×10^{-3}	2.60×10^{-4}	3.62×10^{-4}	4.55×10^{-4}
C-Statistic	5510.72	3230.99	3614.57	3517.77
Degrees of Freedom	5473	4033	3675	3674

Notes: All quoted error bounds correspond to the 90% confidence levels. In the case of the APEC model, the normalization is defined as $(10^{14}/4\pi d^2)\int n_e n_p dV$, where d is the distance to the SNR (in units of centimeters), n_e and n_p are the number densities of electrons and protons respectively (in units of cm^{-3}), and finally $\int dV = V$ is the integral over the entire volume (in units of cm^3). In the case of the power-law model, the normalization is defined as photons keV^{-1} cm^{-2} s^{-1} at 1 keV (see Sect. 5).

Figure 4. Extracted PN, MOS1, and MOS2 spectra of the different regions of G5.9+3.1 as fit with the most probable model (right, table). The residuals to the fits are also shown. In all panels, the PN source spectrum is shown in black, the PN FWC spectrum is shown in red, the MOS1 source spectrum is shown in green, the MOS1 FWC spectrum is shown in blue, the MOS2 source spectrum is shown in cyan, and the MOS2 FWC spectrum is shown in purple. (a – Upper left) Extracted spectra for the whole SNR. (b – Upper right) Extracted spectra for the east rim. (c – Lower left) Extracted spectra for the north rim. (d – Lower right) Extracted spectra for the west rim.

REFERENCES

Onić, D., Filipović, M. D, Bojičić, I., Hurley-Walker, N., et al. 2019, A&A, 625, A93
Pavlović, M. Z., Urošević, D., Vukotić, B., Arbutina, B., & Göker, U. D. 2013, ApJS, 204, 4
Pavlović, M. Z., Dobardzić, A., Vukotić, B., Urošević, D. 2014, Serbian Astronomical Journal, 189, 25
Reich, W., Fürst, E., Reich, P., & Junkes, N. 1988, IAU Colloq., 101, 293

During the work on this paper, the authors were financially supported by the Ministry of Education and Science of the Republic of Serbia through the project 176005 "Emission nebulae: structure and evolution".

1 Department of Astronomy, Faculty of Mathematics, University of Belgrade, Serbia, **2** Western Sydney University, Australia, **3** International Centre for Radio Astronomy Research, Curtin University, Australia, **4** Space Science Center, Department of Earth and Space Sciences, Morehead State University, USA, **5** Max-Planck-Institut für extraterrestrische Physik, Germany, **6** School of Physics, The University of New South Wales, Australia, **7** School of Physical Sciences, The University of Adelaide, Australia, **8** University of Technology Sydney, Australia, **9** Netherlands Institute for Radio Astronomy (ASTRON), The Netherlands, **10** Raman Research Institute, India, **11** International Centre for Radio Astronomy Research (ICRAR), M468, University of Western Australia, Australia, **12** Centre for Astrophysics Research, School of Physics, Astronomy and Mathematics, University of Hertfordshire, College Lane, UK, **13** CSIRO Astronomy and Space Science, Australia, **14** Research School of Astronomy and Astrophysics, Australian National University, Australia, **15** School of Physics, The University of Melbourne, Australia, **16** Shanghai Astronomical Observatory, China